# Supplemental Materials for "Ultrafast modulation of the molten metal surface tension under femtosecond laser irradiation"

Chenhao Li,[1] Hongtao Liang,[1] Yang Yang,[1, *] Zhiyong Yu,[1] Xin Zhang,[1]

Xiangming Ma,[1] Wenliang Lu,[1] Zhenrong Sun,[1] and Ya Cheng[1, †]

[1]*State Key Laboratory of Precision Spectroscopy,*

*School of Physics and Electronic Science,*

*East China Normal University, Shanghai 200241, China*

**TABLE OF CONTENTS**

* yyang@phy.ecnu.edu.cn

† ycheng@phy.ecnu.edu.cn

## I. Simulation Methods

### A. TTM-MD model

The combined two-temperature model molecular-dynamics (TTM-MD) methodology[1–3] is employed to model fully atomistic description of laser interaction with the metal targets. This method combines the continuum description of the laser energy deposition, laser excitation of the electrons and the following electron-phonon relaxation along with ionic density relaxation. The TTM-MD simulation has been currently widely used to reveal important information on the time scales and mechanisms of the melting process occurring under conditions of strong superheating, and the succeeding formation of various complex structures, e.g., porous regions[4] covered by the polycrystalline surface layer[5], and nano-spikes[6], etc.

TTM-MD combines the continuum-level description (two-temperature model[2]) of laser excitation of conduction band electrons followed by electron-phonon equilibration with the MD simulation techniques.

$$\vec{f}_{\text{ion}} = -\frac{\partial U}{\partial \vec{r}_{\text{ion}}} + \vec{f}_{\text{langevin}} - \frac{\nabla p_{\text{e}}}{n_{\text{ion}}} \tag{1}$$

$$C_{\text{e}}\rho_{\text{e}}\frac{\partial T_{\text{e}}}{\partial t} = \frac{\partial\left(\kappa_{\text{e}}\nabla T_{\text{e}}\right)}{\partial z} - g_{\text{p}}\left(T_{\text{e}} - T_{\text{ion}}\right) + g_{\text{s}}T'_{\text{ion}} + \theta\left(z - z_{\text{surface}}\right)I_0\exp\left(-z/l_{\text{skin}}\right) \tag{2}$$

The first term on the right side of Eq.(1) represents the force due to interatomic interactions, the second term is the force due to phonon-electron coupling, and the third term is the so-called hot-electron blast force generated by the electron kinetic pressure[3, 7].

Eq.(2) solves the 1D heat diffusion equation regarding the spatial-temporal evolution of the electron temperature $T_e$. In this equation, $C_e$ is the (per) electron heat capacity, $\rho_e$ is the number density of electrons, and $\kappa_e$ is the electron thermal conductivity. $g_{\text{p}}$ and $g_{\text{s}}$ are responsible for the energy exchange between electronic and atomic subsystems. $g_{\text{p}}$ is the electron-ion coupling coefficient, which determines the rate of energy exchange between the temperatures of the two subsystems ($T_{\text{e}}$ and $T_{\text{ion}}$). $g_{\text{s}}$ is the friction coefficient due to electron stopping effect[8], $T'_{\text{ion}}$ accounts the temperature for the ions moving faster than the electron stopping critical velocity, $v_0$. The laser pulse energy deposition is included through adding a source term - the final term on the right side of Eq.(2), it simulates the excitation

of the conduction-band electrons by the laser pulse, reproduces the exponential decay of laser intensity with optical depth according to the Beer-Lambert-Bouguer law. The incident direction of the laser pulse is along the direction of the target metal surface normal, i.e., $z$ axis direction in the current MD simulation, $\theta\left(z - z_{surface}\right)$ is a step function. $I_0$ is the unit-time (absorbed) laser pulse intensity, the product of $I_0$ and the pulse duration gives the absorbed fluence. $l_{\text{skin}}$ is the effective depth of the laser energy deposition, which includes the optical penetration depth and the effective depth of the "ballistic" energy transport before the thermalization of the excited electrons[4, 9, 10].

## B. Simulation details

- *Interatomic potentials*

We focus on the surface of three pure molten metals, i.e., Al, Ti, and Ni, at temperatures near $T_{\text{m}}$. The TTM-MD simulations are based on the embedded-atom-method (EAM) potentials for Al and Ti by Zope and Mishin[11], and for Ni by Pun and Mishin[12]. The potentials provide adequate reasonable descriptions of thermodynamic properties (e.g., surface tension, see Section IV below) of the molten metals relevant to the simulation of laser-induced processes under a relatively weak fluence. In particular, the $T_{\text{m}}$ determined in crystal-melt coexistence simulations for Al, Ti, and Ni are 870K, 1531K, and 1675K, which are consistent well with the experimental values of 933K, 1941K, and 1728K, respectively[13, 14].

- *Coefficients for implementing TTM-MD*

The TTM-MD simulations are performed using LAMMPS[15]. Through investigation and preliminary calculations, we have clarified the following physical parameters necessary for TTM-MD simulation calculations, including but not limited to electron heat capacity, electron density, electron thermal conductivity, electron thermal diffusion coefficient, electro-phonon coupling coefficients, etc. The specific information of the model used in the simulations of laser interaction with the three molten metals are provided as follows.

The electron temperature dependences of the electron heat capacity $C_{\text{e}}(T_{\text{e}})$, which accounts for the thermal excitation from the electron states below the Fermi level, is expressed as follows,

$$C_{\text{e}}(T_{\text{e}}) = C_0 + \left[a_0 + a_1 \tilde{T}_{\text{e}} + a_2 \tilde{T}_{\text{e}}^{\,2} + a_3 \tilde{T}_{\text{e}}^{\,3} + a_4 \tilde{T}_{\text{e}}^{\,4}\right] \mathbf{e}^{-(C_1 \tilde{T}_{\text{e}})^2}, \tag{3}$$

3

in which, $\tilde{T}_e = T_e/1000$. The parameters in Eq.3 for the three metals are listed in Tab.SI, which are obtained from fitting the reported $C_e(T_e)$ curves for Al, Ti, and Ni in the Ref.[16], in the electron temperature range from 250K to 50,000K.

The electron thermal conductivity $\kappa_e(T_e)$ is determined from Eq.(4), by assuming it is simply proportional to the electron heat capacity $C_e(T_e)$,

$$\kappa_e(T_e) = D_e \rho_e C_e(T_e), \tag{4}$$

in which, the pre-factor $D_e$ is the electronic thermal diffusion coefficient. The magnitudes of $D_e$ for the three metals investigated here are estimated (see Tab.SI) under the low temperature limit of the Drude theory[17], in which $\kappa_e$, $C_e$, and $T_e$ are approximately linearly dependent on each other.

In order to simulate the atomic subsystem of the TTM-MD being effectively embedded in the bath of electrons, the coarse-grained electronic temperature (CET) grids along 1D are employed. According to Duffy and Rutherford[8, 18], $g_p$ and $g_s$ have the following expressions,

$$g_p = \frac{3Nk_B\Gamma_p}{\Delta V m}, \tag{5}$$

$$g_s = \frac{3N'k_B\Gamma_s}{\Delta V m}, \tag{6}$$

in which, $k_B$ is Boltzmann's constant, $m$ is the mass of atom, $\Delta V = A\Delta z$ is the volume of the CET grid, $A$ is the cross-section area. $N$ is the number of atoms in the CET grid. $N'$ is the number of atoms with velocities higher than the electron stopping critical velocity, $v_0$. Note that, we follow the recipe of Duffy and Rutherford, and define the electronic stopping for particles with kinetic energy no less than a cut-off value, $E_c$, taken to be twice the cohesive energy. As listed in Tab.SI, $g_p$ and $\Gamma_p$ for the three metals are taken from the Ref.[16], the electronic stopping coefficients $\Gamma_s$ for the three metals are obtained directly from the electronic stopping curves of SRIM database[19, 20].

For the 1D system of the electron temperature variation, the hot-electron blast force term $\nabla p_e$ can be rewritten as,

$$\nabla_z p_e = \left[ \frac{C_e T_e(z)\lambda}{(z+\lambda)^2} + \frac{z}{z+\lambda} \frac{(C_e T_e)_{z+\Delta z} - (C_e T_e)_z}{\Delta z} \right], \tag{7}$$

Tab.S I. Summary of the coefficients for implementing of the TTM-MD simulations

| | Al | Ti | Ni |
|---|---|---|---|
| $C_0$ (eV/K) | $9.89\times10^{-5}$ | $10.30\times10^{-5}$ | $17.95\times10^{-5}$ |
| $a_0$ (eV/K) | $-9.83\times10^{-5}$ | $-10.15\times10^{-5}$ | $-17.19\times10^{-5}$ |
| $a_1$ (eV/K$^2$) | $3.61\times10^{-7}$ | $2.50\times10^{-6}$ | $9.65\times10^{-7}$ |
| $a_2$ (eV/K$^3$) | $-3.65\times10^{-9}$ | $-1.65\times10^{-8}$ | $-4.93\times10^{-9}$ |
| $a_3$ (eV/K$^4$) | $1.41\times10^{-11}$ | $4.19\times10^{-11}$ | $-1.01\times10^{-11}$ |
| $a_4$ (eV/K$^5$) | $3.92\times10^{-14}$ | $-3.87\times10^{-14}$ | $3.88\times10^{-14}$ |
| $C_1$ (1/K) | $5.55\times10^{-3}$ | $3.64\times10^{-3}$ | $5.07\times10^{-3}$ |
| $\rho_{\mathrm{e}}$ (1/Å$^3$) | 0.181 | 0.113 | 0.183 |
| $\rho_{\mathrm{ion}}$ (1/Å$^3$) | 0.060 | 0.057 | 0.091 |
| $D_{\mathrm{e}}$ (Å$^2$/ps) | 311767 | 4599 | 5261 |
| $\Gamma_{\mathrm{p}}$ (g/ps) | 0.2 | 3.5 | 0.5 |
| $\Gamma_{\mathrm{s}}$ (g/ps) | 31.2 | 44.7 | 34.7 |
| $v_0$ (Å/ps) | 69.6 | 62.5 | 54.4 |
| $\lambda$ (Å) | 189 | 85 | 59 |
| $Z$ (1/(Å$^2$ps)) | 0.57 | 0.36 | 0.57 |
| $S_a$ (Å$^2$) | 3.78 | 5.16 | 3.75 |

in which, $\lambda$ is the electron mean free path. The specific values for $\lambda$ for the three investigated metals listed in Tab.SI are taken from Ref.[21 and 22].

- *Simulation setup*

The simulations presented are performed for molten Al, Ti and Ni surfaces irradiated with laser pulses of two different pulse durations (or pulse widths), i.e., 200 fs and 50 ps. The (absorbed) laser pulse intensities for the two laser pulse durations cases, are 80 mJ/(cm$^2$ps) and 0.32 mJ/(cm$^2$ps), respectively, yielding a same absorbed fluence of 16 mJ/cm$^2$. This fluence is chosen so that no void nucleation, spallation, or disintegration of the liquid surfaces occurs during the thermal expansion.

As shown in the schematic diagram of the simulation system in Fig.S1, the simulation

cells employ the periodic boundary condition (PBC) along the directions ($x$ and $y$) parallel to the molten metal surfaces, to model a small portion of the irradiated planar surfaces in the laser spot. The electronic temperature simulation cell has dimension of 75Å×75Å×1400Å, it extends beyond the initial atomic domain which owns the identical cross-sectional dimensions. The cell dimension along discretized into 700 (1D) CET grids, with the grid size $\Delta z$=2Å. The included molten liquids modeled by atomistic TTM-MD is around 1000 in length along $z$, with around 350,000 Al particles, or 303,000 Ti particles, or 517,000 Ni particles. The empty space in front of the target surface is necessary and sufficient large to accommodate the thermal expansion.
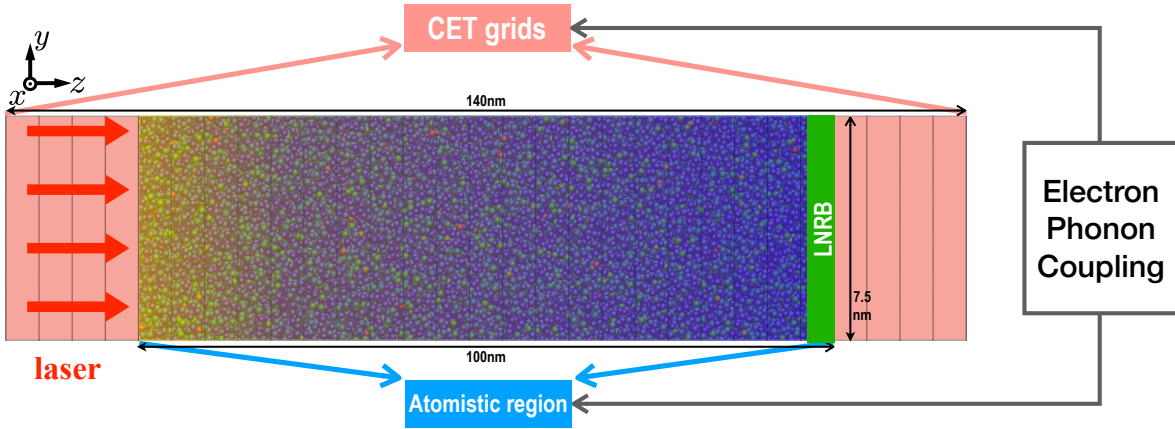


Fig.S 1. Schematic diagram of the electronic system and the atomic system coupling in the TTM-MD simulation of the liquid metal surfaces under the irradiation of the laser pulse. The laser pulse is directed along the $z$ axis, from the left of the sketch. The empty space in front of the target surface is necessary and sufficient large to accommodate the thermal expansion. Langevin nonreflecting boundary (LNRB) condition is employed absorb the laser-induced pressure wave and undermine its reflective propagation[23]. The region beyond LNRB boundary is modeled by the original TTM formulation, mimicking the heat transfer into the deeper bulk part of the molten melts.

The simulation time step is set as 1 fs. Before applying laser irradiation, the well equilibrated molten metal slab with two surfaces are prepared from the constant volume, constant temperature ($NVT$) MD simulation runs over 150 ns, at 0.95 $T_{\mathrm{m}}$ of each EAM metal. We follow the initial $NVT$ runs with the laser irradiation TTM-MD runs. To measure

the laser-induced non-equilibrium spatial-temporal evolution of the surface thermodynamic properties, the CET grid temperature, per particle properties (i.e., coordinates, velocities, and stress tensors) are collected each 100 TTM-MD steps, for a time lasting until two temperatures converge, i.e., 30 ps for the 200 fs laser pulse cases, or 150 ps for the 50 ps laser pulse cases. To improve the statistics, 500 initial configurations from $NVT$ simulations are chosen to start the laser irradiation TTM-MD simulations. To ensure independence, these 500 starting configurations are separated by 0.5 ns, therefore, we have 500 independent irradiated surfaces for each molten metals from which to calculate the interfacial property evolutions with high-precision and determine the statistical uncertainty.

- *Semi-infinite boundary condition*

The propagation of laser-induced pressure waves towards the bulk interior of the irradiated materials can be mimicked with employing the Langevin nonreflecting boundary (LNRB) condition[23], so that reflections of laser-induced pressure waves from the back side of the liquid metal target do not play role in the modulation of the surface stress field in the current study. We use a width of three monoatomic layers as the LNRB layer to ensure the stable behavior of the boundary condition. The equation of motion for each atom in this LNRB layer is expressed in the form of Langevin dynamics equation with a dumping constant $ZS_a$, here $Z$ is the phonon impedance coefficient of the material, and $S_a$ is the total area of the boundary divided by the number of boundary atoms, see in Tab.SI. In the region beyond LNRB boundary, the electronic and atomic subsystems are modeled by the original TTM formulation[24]. This region mimics the heat transfer into the deeper bulk part of the molten melts, it serves as a buffer to ensure reasonable two-temperature evolution. Due to the low dose irradiation employed here, a size of 20nm for this region is chosen to ensure a negligible temperature change in the interested time-windows after the laser irradiation.

## II. Computational Methods

In this section, we describe the computational methods for the key thermodynamic quantities across the liquid-vapor interface which undergoes symmetry broken in the particle packing. We perform the calculation for the instantaneous interfacial profiles, e.g., density profiles, pressure components profiles and stress profiles, by firstly collecting the fine-grained particle densities and pressure components defined in Eq.(8) during the equilibrium $NVT$

7

and non-equilibrium TTM-MD simulations.

The determination of the pressure tensor $p_{\alpha\beta}$ uses the so-called virial method, in which the per-particle virial stress tensors (in units of pressure×volume) are calculated by adding half of a pairwise interaction virial contribution to the kinetic energy (which subtracts the component due to local collective/streaming velocities[25]),

$$s_i^{\alpha\beta}(t) = -\left[ m[v_{i\alpha}(t) - u_\alpha(r_i, t)][v_{i\beta}(t) - u_\beta(r_i, t)] + \frac{1}{2}\sum_{j=1}^{N_n}\left[ r_{i_\alpha}(t)f_{i_\beta}(t) + r_{j_\alpha}(t)f_{j_\beta(t)} \right] \right] \quad (8)$$

where $\alpha$, $\beta$ take on values $x, y, z$, $v_i$ is the velocity of particle $i$. $r_i$ and $r_j$ are the positions of particle $i$ and $j$ in the pairwise interaction. $u(r_i, t)$ is the local collective/streaming velocity of the fluid at position $r_i$. $f_i$ and $f_j$ are the forces on the two particles. $N_n$ is the number of particle $i$'s neighboring particles. This definition is applicable to calculate the pressure components and stress fields of the non-equilibrium surface systems engaged with pressure wave propagations and rapid expansions.

The instantaneous fine-grained density profile across the molten metal surface at time $t$, $\rho(z, t)$, is computed as the average number of atoms in each discrete bin of spacing $\delta z$ divided by the volume of the bin, $A\delta z$,

$$\rho(z, t) = \frac{\langle N_{z,t} \rangle}{A\delta z}, \quad (9)$$

where $\langle N_{z,t} \rangle$ is the average number of atoms in the discrete bin, over 500 samples from 500 replica simulation runs. The discrete bin spacing is chosen as $\delta z$=0.1Å.

The instantaneous fine-grained pressure components profiles along the surface normal, $p_{\alpha\beta}(z, t)$, are determined in fine-graining $z$ axis with bin size $\delta z$, and calculated as the sum of the negative per-particle stress tensors $s_i^{\alpha\beta}$ divided by bin volume and the summation run over $N_{z,t}$ particles located between $z$ and $z + \delta z$,

$$p_{\alpha\beta}(z, t) = -\frac{\left\langle \sum_i^{N_{z,t}} s_i^{\alpha\beta}(z, t) \right\rangle}{A\Delta z}, \quad (10)$$

here $A$ is the cross-section area, and again the bracket average over 500 instantaneous trajectory samples from 500 replica simulation runs, at the same $t$ value.

The instantaneous fine-grained stress profile is defined as the difference between the fine-grained normal ($p_N$) and transverse components ($p_T$) of the pressure tensor,

$$S(z,t) = p_{\mathrm{N}}(z,t) - p_{\mathrm{T}}(z,t), \tag{11}$$

$$p_{\mathrm{N}}(z,t) = p_{zz}(z,t), \tag{12}$$

$$p_{\mathrm{T}}(z,t) = \frac{1}{2}\left[p_{xx}(z,t) + p_{yy}(z,t)\right]. \tag{13}$$

The calculation of the dynamic surface tension, $\gamma(t)$, uses the mechanical definition of the equilibrium surface tension via the Kirkwood-Buff equation[26], by integrating the stress profile over the entire length of the simulation cell,

$$\gamma(t) = \int_{z_{\mathrm{lo}}}^{z_{\mathrm{hi}}} S(z,t)\mathrm{d}z, \tag{14}$$

in which, $L_z = z_{\mathrm{hi}} - z_{\mathrm{lo}}$ is the system dimension in $z$. Practically, the numerical integration employ the Simpson rule, the systematic error arises from the numerical integration is found smaller than the statistical error.

Strictly speaking, the mechanical definition of the surface tension is valid only for a liquid-vapor interfacial system under a hydrostatic equilibrium state[26, 27]. One might choose to define a dynamic (or instantaneous) surface tension by Eq.(14) in the equilibrium state, then the time-averaged dynamic surface tension over all instantaneous samples would reduce to the thermodynamic equilibrium surface tension. During a non-equilibrium process, as in the current study, we need a quantitative way (or terminology) to count the liquid-vapor interface excess stress (or stress field) within the highly non-equilibrium state before the magnitude of the dynamic surface tension relaxes to the value of the equilibrium surface tension. Note that experimental and computational studies have focused on the dynamic liquid surface tension during the non-equilibrium processes. For example, the computational study carried out by Lukyanov and Likhtman utilized the same equation (Eq.(14)) to calculate the variation of the dynamic surface tension of a liquid droplet during its (non-equilibrium) re-establishment after manual creation of fresh bare interface with the bulk arrangement of particles by removing all particles of the interfacial layer[28]. In another example, Hauner et al. measured the dynamic surface tension of water droplets and its correlation with the dynamic adsorption effects of protons experimentally by determining the diameter of the liquid bridge[29].

For an equilibrium liquid-vapor interface system, the bulk liquid and vapor phase outside the interface area naturally satisfy the hydrostatic pressure condition with zero stresses.

9

Meanwhile, there are several layers of particles in the liquid-vapor interfacial transition region, where the stresses are not equal to 0. The stress distribution functions in Fig.3 ($t = 0$ ps) in the main text and many other stress profile plots listed below show that particles in this local region are intrinsically non-hydrostatic. In contrast to the non-hydrostatic crystal-melt interface system, in which the melt phase coexists with the bulk crystal phase in the homogeneous non-hydrostatic condition by applying positive/negative strain to the crystal phase[30]. In this type of interface, the calculation of the interface excess stress relies on the choice of the Gibbs dividing surface, and the Eq.(14) is not applicable. Of course, it is almost impossible for a liquid-vapor interface system to have the bulk liquid phase in a homogeneous non-hydrostatic condition. In the current study, the stress field variation induced by the fs-laser irradiation modifies the local non-hydrostatic condition at the nearby interfacial region ranging by several nm. This effect acts as a shock wave propagating towards the bulk interior of the liquid phase. This shock wave gradually weakens as it propagates, maintaining a width of several nanometers. Within the interested non-equilibrium period of a few tens of ps, the bulk stress away from the surface region is always zero, and no homogeneous bulk non-hydrostatic condition is formed. During the whole process, the stress field change is reflected in the broadening of the local non-hydrostatic region near the interface, and the dynamic stress profiles are not substantially deviating from the equilibrium liquid-vapor interface stress field. No homogeneous bulk non-hydrostatic condition is formed. Thus no violation of hydrostatic pressure conditions. Therefore, we choose to define the dynamic surface tension utilizing the Eq.(14).

To gain quantitative insight of the local contributions, we separate the integration in Eq.(14) into two components. In this way, the contribution of the outermost atomic layer (positive stress peak)[31] ($\gamma_{\text{top}}$), is distinguished from the contribution of the rest of the surface, i.e., subsurface layers ($\gamma_{\text{sub}}$),

$$\gamma(t) = \gamma_{\text{top}}(t) + \gamma_{\text{sub}}(t) = \int_{z_{\text{lo}}}^{z_1(t)} S(z,t)\mathrm{d}z + \int_{z_1(t)}^{z_{\text{hi}}} S(z,t)\mathrm{d}z, \tag{15}$$

here, $z_1(t)$ is the position where the stress change sign from positive to negative at the end of the positive stress peak in the instantaneous stress profile, $S[z_1(t), t] = 0$.

### III. Supplemental Data

This section covers the supplemental data supporting the main text, including: (i) ad-

10

ditional TTM-MD simulation snapshots, electron and ion temperature evolutions, see in Fig.S2; (ii) Temporal and spatial evolution of the fine-grained density $\rho(z,t)$ and stress $S(z,t)$ profiles across the three molten Al, Ti and Ni surfaces, irradiated with (200 fs or 50 ps) laser pulse at the same amount of absorbed fluence of 16 mJ/cm$^2$, see in Fig.S3,4,5,6,7; (iii) Temporal evolution of two contributing components of the dynamic surface tension, represented with the differences ($\delta\gamma_{\text{top}}(t) = \gamma_{\text{top}}(t) - \gamma_{0\text{top}}$, $\delta\gamma_{\text{sub}}(t) = \gamma_{\text{sub}}(t) - \gamma_{0\text{sub}}$) between the temporal instantaneous values and the equilibrium values, normalized by $\gamma_0$, for the three molten surfaces irradiated with the 50 ps laser pulse, see in Fig.S8; (iv) Contour plots of fine-grained profiles of the normal ($p_{\text{N}}(z,t)$) and transverse components ($p_{\text{T}}(z,t)$) of the pressure tensor, and the stress ($S(z,t)$) of the three molten metal surfaces irradiated with the 50 ps laser pulse, see in Fig.S9.

## IV. Supporting Information (Equilibrium Systems)

A. Equilibrium surface tension

We measure the mean density and stress profiles, as well as the temperature dependent surface tensions for the equilibrium state molten metal surfaces, from a series of $NVT$ simulations. In each equilibrium simulation, liquid metal slabs containing two open liquid-vapor surfaces in a rectangular simulation box with the PBC condition being applied along cross-sectional dimensions, are equilibrated over 5 milliion MD steps (time step 1fs). The dimensions of the cross section are identical to the TTM-MD simulation mentioned above, there are around 20,000 metal particles in the liquid slabs. The interfacial profiles and the surface tension are calculated following the method described in the Refs.[32, 33].

The obtained mean density $\rho(z,T)$ and stress profiles $S(z,T)$ across the surfaces at six increasing temperatures, are depicted in the plots of Fig.S10. Temperature dependences of the equilibrium surface tensions for the three metal systems are shown in Fig.S11 (a1-c1). The calculated surface tension as the function of temperature, for each metal surface, shows a nearly linear decrease as temperature increases. Through linear least square fittings, it is found that the equilibrium surface tensions are decreasing with temperatures at estimated rates of 0.075 mN/(m·K), 0.118 mN/(m·K), and 0.234 mN/(m·K), for Al, Ti, and Ni, respectively. The $\gamma_0$ (appear in the main text), are calculated as 593(2) mN/m, 1005(2) mN/m, and 892(4) mN/m, for the equilibrium Al, Ti, and Ni liquid surfaces before laser irradiation.

Numbers in parentheses are 95% confidence errors for the last digits shown.

By comparing with the experimental measurements[34–36], the decreasing rates for the three molten metal surface tensions modeled by the EAM potentials, are lower than the experiment measurements by approximately 0.1 mN/(m·K). For example, one gets the decreasing rate of 0.185 mN/(m·K) for Al[34], 0.238 mN/(m·K) for Ti[35], and 0.330 mN/(m·K) for Ni[36]. The equilibrium surface tension values around the melting temperature reasonably agree with the experimental values, i.e., the calculated $\gamma_0$ are smaller (yet less than a factor of 2) than that reported in previous experimental studies at $T = T_{\mathrm{m}}$, 880 mN/m for Al[34], 1640 mN/m for Ti[35], and 1760 mN/m for Ni[36].

The contribution of positive stress peak $\gamma_{\mathrm{top}}(T)$ of the equilibrium surface tension as the function of temperature, as well as the subsurface layers, $\gamma_{\mathrm{sub}}(T)$ are plotted in Fig.S11 (a2-c2).

## B. Liquid density relaxation time

We measure the liquid density relaxation time $\tau_{k_1,T_{\mathrm{m}}}$ ($\tau$, for simplicity in the main text) for the three molten metals in bulk $NpT$ simulations, sampling 4,000 metal particles at ambient pressure, $T = T_{\mathrm{m}}$. The subscript $k_1$ refers to the first peak wave vector (modulus) in the static structure function $\mathbf{S}(|\vec{k}|)$ of the liquids. We run 10,000,000 MD steps (1 fs time step) for each bulk molten metal, use over half of them for collecting averages (using block averages) for the 50 replica computations of the intermediate scattering functions and the dynamic structure factors.

Liquid density relaxation time $\tau_{k_1,T_{\mathrm{m}}}$ is defined as the inverse half-width of the dynamic structure factor, $\mathbf{S}(k_1,\omega)$, at the given wave vector, i.e., $k_1$. The calculated static and dynamic structure factors for the three metals investigated are plotted in the Fig.S12, and the corresponding calculation expressions are as follows,

$$\mathbf{S}(|\vec{k}|) = \frac{1}{N}\langle\sum_{i=1}^{N}\sum_{j=1}^{N}\exp[-i\vec{k}\cdot(\vec{r_i} - \vec{r_j})]\rangle, \tag{16}$$

$$\mathbf{F}(|\vec{k}|,t) = \frac{1}{N}\langle\sum_{i=1}^{N}\sum_{j=1}^{N}\exp[-i\vec{k}\cdot(\vec{r_i}(t) - \vec{r_j}(0))]\rangle, \tag{17}$$

$$\mathbf{S}(|\vec{k}|,\omega) = \frac{1}{2\pi}\int_{-\infty}^{+\infty}\mathbf{F}(|\vec{k}|,t)\exp(i\omega t)\mathrm{d}t, \tag{18}$$

where $\mathbf{F}(\vec{k}, t)$ is the intermediate scattering function. The measured values of $\tau$, for the molten Al, Ti, and Ni, are $\tau_{\mathrm{Al}} = 0.57(6)$ ps, $\tau_{\mathrm{Ti}} = 0.56(4)$ ps, and $\tau_{\mathrm{Ni}} = 0.53(4)$ ps, respectively. Numbers in parentheses are 95% confidence errors for the last digits shown.

**Additional References**

[1] D. S. Ivanov and L. V. Zhigilei, "Effect of pressure relaxation on the mechanisms of short-pulse laser melting," Phys. Rev. Lett. **91**, 105701 (2003).

[2] D. S. Ivanov and L. V. Zhigilei, "Combined atomistic-continuum modeling of short-pulse laser melting and disintegration of metal films," Phys. Rev. B **68**, 064114 (2003).

[3] J. K. Chen, D. Y. Tzou, and J. E. Beraun, "A semiclassical two-temperature model for ultrafast laser heating," Int. J. Heat Mass Transf. **49**, 307–316 (2006).

[4] C. P. Wu, M. S. Christensen, J.-M. Savolainen, P. Balling, and L. V. Zhigilei, "Generation of subsurface voids and a nanocrystalline surface layer in femtosecond laser irradiation of a single-crystal Ag target," Phys. Rev. B **91**, 035413 (2015).

[5] X. Sedao, M. V. Shugaev, C. P. Wu, T. Douillard, C. Esnouf, C. Maurice, S. Reynaud, F. Pigeon, F. Garrelie, L. V. Zhigilei, *et al.*, "Growth twinning and generation of high-frequency surface nanostructures in ultrafast laser-induced transient melting and resolidification," ACS Nano **10**, 6995–7007 (2016).

[6] C. P. Wu and L. V. Zhigilei, "Nanocrystalline and polyicosahedral structure of a nanospike generated on metal surface irradiated by a single femtosecond laser pulse," J. Phys. Chem. C **120**, 4438–4447 (2016).

[7] L. A. Falkovsky and E. G. Mishchenko, "Electron-lattice kinetics of metals heated by ultrashort laser pulses," J. Exp. Theor. Phys. **88**, 84–88 (1999).

[8] D. M. Duffy and A. M. Rutherford, "Including the effects of electronic stopping and electron-ion interactions in radiation damage simulations," J. Phys. Condens. Mat. **19**, 016207 (2006).

[9] C. Y. Shih, M. V. Shugaev, C. P. Wu, and L. V. Zhigilei, "Generation of subsurface voids, incubation effect, and formation of nanoparticles in short pulse laser interactions with bulk metal targets in liquid: molecular dynamics study," J. Phys. Chem. C **121**, 16549–16567 (2017).

[10] C. Y. Shih, R. Streubel, J. Heberle, A. Letzel, M. V. Shugaev, C. P. Wu, M. Schmidt, B. Gökce, S. Barcikowski, and L. V. Zhigilei, "Two mechanisms of nanoparticle generation in picosecond laser ablation in liquids: the origin of the bimodal size distribution," Nanoscale **10**, 6900–6910 (2018).

[11] R. Zope and Y. Mishin, "Interatomic potentials for atomistic simulations of the Ti-Al system," Phys. Rev. B **68**, 024102 (2003).

[12] G. P. Pun and Y. Mishin, "Development of an interatomic potential for the Ni-Al system," Philos. Mag. **89**, 3245–3267 (2009).

[13] W. J. Zhang, Y. F. Peng, and Z. L. Liu, "Molecular dynamics simulations of the melting curve of NiAl alloy under pressure," AIP Adv. **4**, 057110 (2014).

[14] Q. Bizot, O. Politano, A. A. Nepapushev, S. G. Vadchenko, A. S. Rogachev, and F. Baras, "Reactivity of the Ti-Al system: Experimental study and molecular dynamics simulations," J. Appl. Phys. **127**, 145304 (2020).

[15] S. Plimpton, "Fast parallel algorithms for short-range molecular dynamics," J. Comput. Phys. **117**, 1–19 (1995).

[16] Z. Lin, L. V. Zhigilei, and V. Celli, "Electron-phonon coupling and electron heat capacity of metals under conditions of strong electron-phonon nonequilibrium," Phys. Rev. B **77**, 075133 (2008).

[17] G. E. Norman, S. V. Starikov, V. V. Stegailov, I. M. Saitov, and P. A. Zhilyaev, "Atomistic modeling of warm dense matter in the two-temperature state," Contrib. Plasm. Phys. **53**, 129–139 (2013).

[18] A. M. Rutherford and D. M. Duffy, "The effect of electron-ion interactions on radiation damage simulations," J. Phys. Condens. Mat. **19**, 496201 (2007).

[19] R. E. Stoller, M. B. Toloczko, G. S. Was, A. G. Certain, S. Dwaraknath, and F. A. Garner, "On the use of srim for computing radiation damage exposure," Nucl. Instrum. Meth. B **310**, 75–80 (2013).

[20] J. F. Ziegler, M. D. Ziegler, and J. P. Biersack, "Srim–the stopping and range of ions in matter (2010)," Nucl. Instrum. Meth. B **268**, 1818–1823 (2010).

[21] G. G. Fuentes, E. Elizalde, F. Yubero, and J. M. Sanz, "Electron inelastic mean free path for Ti, TiC, TiN and TiO2 as determined by quantitative reflection electron energy-loss spectroscopy," Surf. Interface Anal. **33**, 230–237 (2002).

[22] D. Gall, "Electron mean free path in elemental metals," J. Appl. Phys. **119**, 085101 (2016).

[23] M. V. Shugaev, I. Gnilitskyi, N. M. Bulgakova, and L. V. Zhigilei, "Mechanism of single-pulse ablative generation of laser-induced periodic surface structures," Phys. Rev. B **96**, 205429 (2017).

[24] S. I. Anisimov, B. L. Kapeliovich, and T. L. Perelman, "Electron emission from metal surfaces exposed to ultrashort laser pulses," Sov. Phys.-JETP **39**, 375 (1974).

[25] B. D. Todd, D. J. Evans, and P. J. Daivis, "Pressure tensor for inhomogeneous fluids," Phys. Rev. E **52**, 1627–1638 (1995).

[26] J. G. Kirkwood and F. P. Buff, "The statistical mechanical theory of surface tension," J. Chem. Phys. **17**, 338–343 (1949).

[27] R Evans, "A pseudo-atom theory for the surface tension of liquid metals," J. Phys. C **7**, 2808–2830 (1974).

[28] A. V. Lukyanov and A. E. Likhtman, "Relaxation of surface tension in the free-surface boundary layer of simple lennard-jones liquids," J. Chem. Phys. **138**, 034712 (2013).

[29] I. M. Hauner, A. Deblais, J. K. Beattie, H. Kellay, and D. Bonn, "The dynamic surface tension of water," J. Phys. Chem. Lett. **8**, 1599–1603 (2017).

[30] T. Frolov and Y. Mishin, "Effect of nonhydrostatic stresses on solid-fluid equilibrium. ii. interface thermodynamics," Phys. Rev. B **82**, 174114 (2010).

[31] Z. F. Yuan, H. T. Liang, C. J. Xia, B. B. Laird, X. G. Gong, and Y. Yang, "in preparation," (2022).

[32] H. T. Liang, B. B. Laird, M. Asta, and Y. Yang, "In-plane characterization of structural and thermodynamic properties for steps at faceted chemically heterogeneous solid/liquid interfaces," Acta Mater. **143**, 329–337 (2018).

[33] W. L. Lu, H. T. Liang, X. M. Ma, Z. F. Yuan, X. Zhang, Z. Liang, and Y. Yang, "Atomistic simulation study of the fcc and bcc crystal-melt interface stresses," Surf. Interfaces **28**, 101639 (2022).

[34] J. M. Molina, R. Voytovych, E. Louis, and N. Eustathopoulos, "The surface tension of liquid aluminium in high vacuum: The role of surface condition," Int. J. Adhes. Adhes. **27**, 394–401 (2007).

[35] K. Zhou, H. P. Wang, J. Chang, and B. Wei, "Experimental study of surface tension, specific heat and thermal diffusivity of liquid and solid titanium," Chem. Phys. Lett. **639**, 105–108

(2015).

[36] H. P. Wang, J. Chang, and B. Wei, "Measurement and calculation of surface tension for undercooled liquid nickel and its alloy," J. Appl. Phys. **106**, 033506 (2009).
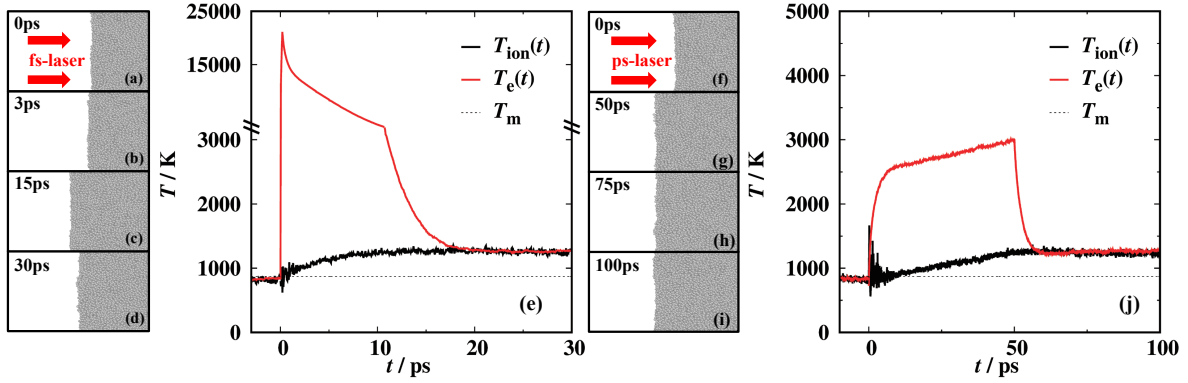
Fig.S 2. Selected snapshots from TTM-MD simulation of a representative the molten metal (Al) surface irradiated with 200 fs laser pulse (panel (a)-(d)), and 50 ps laser pulse (panel (f)-(i)) at an absorbed fluence of 16 mJ/cm². The laser pulse is directed along the $z$ axis, perpendicular to the molten metal surfaces from the left of plots. Temporal evolutions of the electron ($T_e(t)$, red) and ion temperatures ($T_{ion}(t)$, black) for the front 1.5 nm of the fs laser (e) and ps laser (j) irradiated surfaces. For the molten Ti and Ni surfaces irradiated with the same fs laser pulse and ps laser pulse, similar fashions of the surface expansion and the temperature profiles are observed.
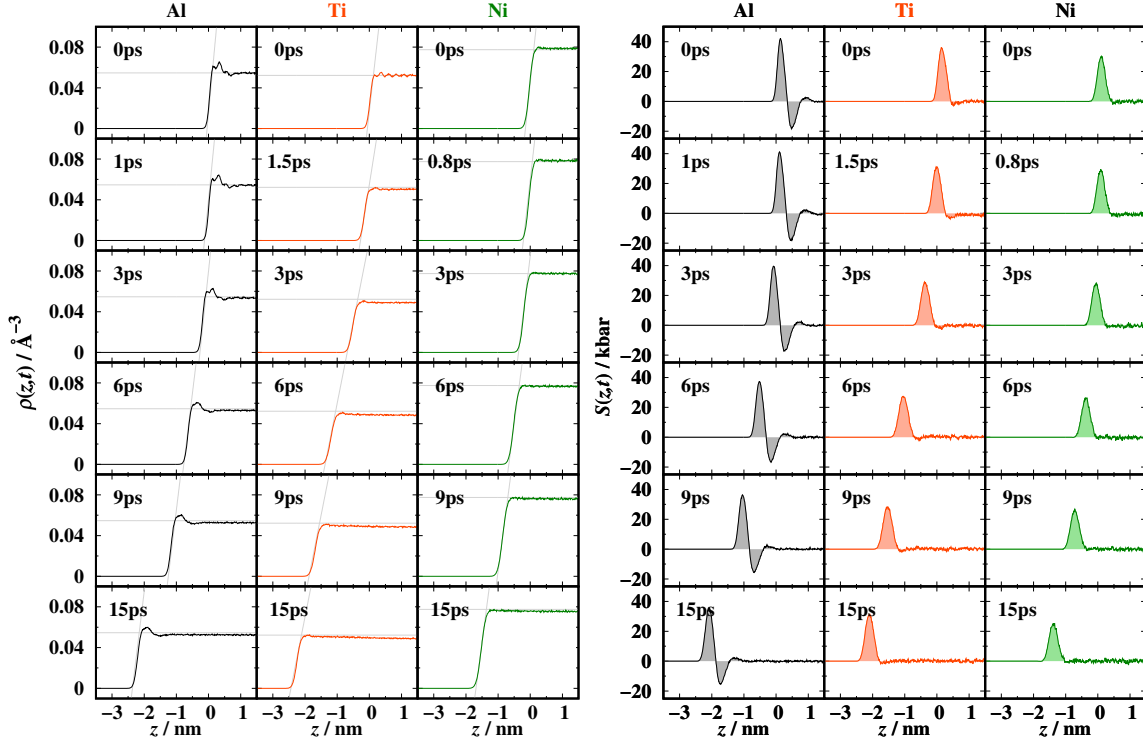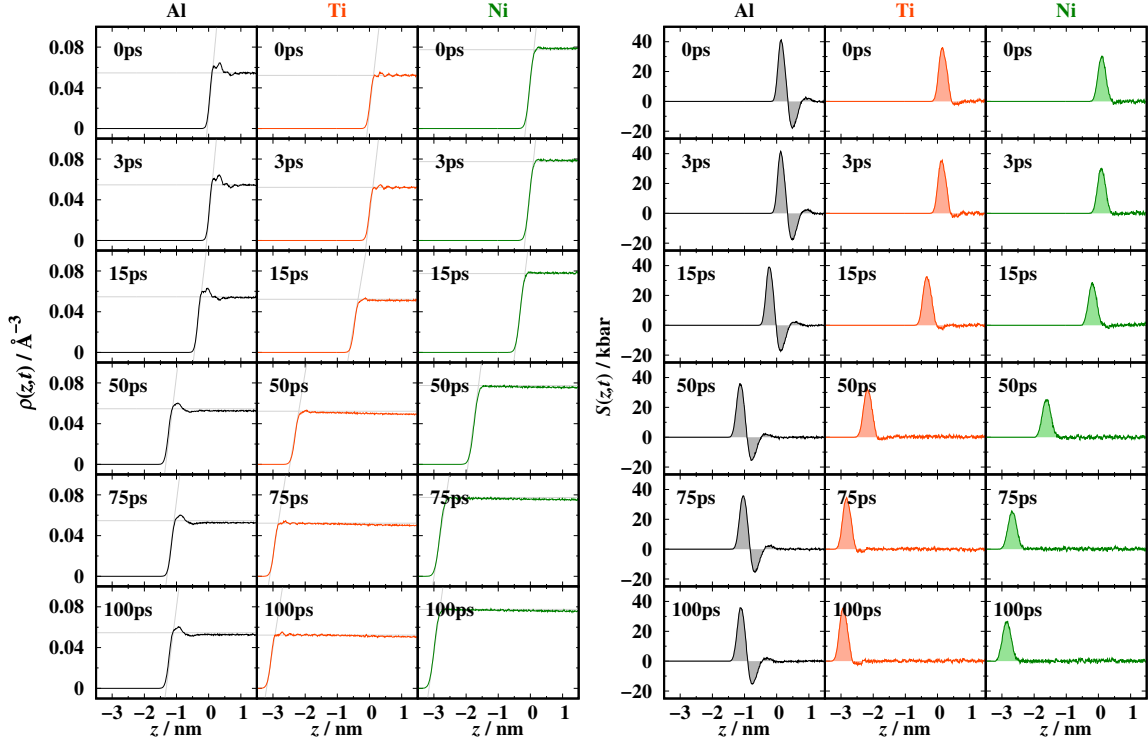
Fig.S 3. Evolution of the density $\rho(z,t)$ and stress $S(z,t)$ profiles across the three molten Al, Ti and Ni surfaces, irradiated with a 200 fs laser pulse at an absorbed fluence of 16 mJ/cm$^2$. Surfaces expand along $-z$ direction, opposite to the laser incident direction. $z = 0$ corresponds to the Gibbs dividing surface position (defined with zero excess particle number density) of each equilibrium molten metal surfaces before laser irradiation. The two thin solid lines in the panels with $\rho(z,t)$ profile mark the magnitude of the equilibrium bulk liquid density at $T = 0.95T_\mathrm{m}$, and the gradient of the liquid surface, respectively. The shaded area in the $S(z,t)$ profile corresponds to the implementing of the Kirkwood-Buff equation, Eq.(14).

Fig.S 4. Evolution of the density $\rho(z, t)$ and stress $S(z, t)$ profiles across the three molten metal surfaces, irradiated with a 50 ps laser pulse at same amount of absorbed fluence of 16 mJ/cm$^2$. The presentation is as in Fig.S3.
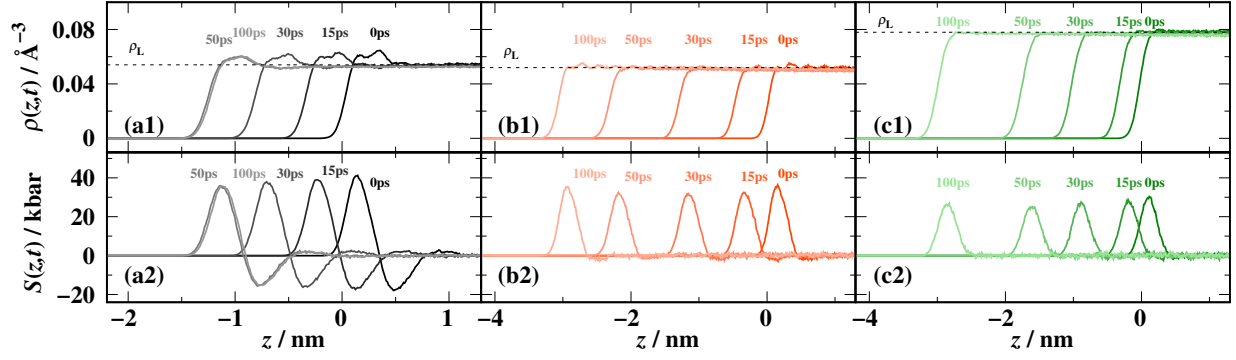
Fig.S 5. Evolution of the density $\rho(z,t)$ and stress $S(z,t)$ profiles across the 50 ps laser pulse irradiated molten Al (a1-a2), Ti (b1-b2) and Ni (c1-c2) surfaces at a few selected times. Surfaces expand along $-z$, opposite to the laser incident direction. $z = 0$ corresponds to the Gibbs dividing surface position (GDS for short, defined with zero excess particle number density) of each equilibrium molten metal surfaces before laser irradiation.
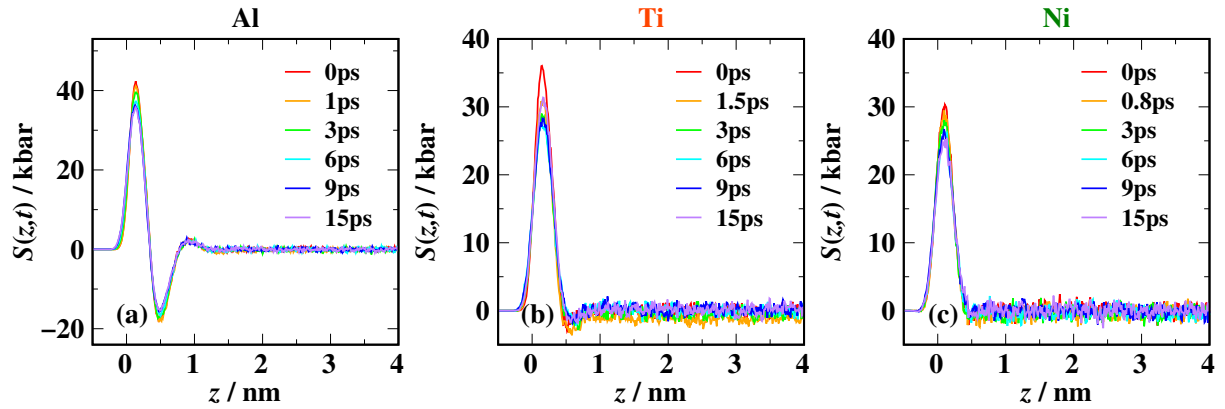


Fig.S 6. 200 fs laser pulse irradiated molten surfaces. The selected stress $S(z,t)$ profiles are aligned by the GDS of the irradiated liquid surfaces at each time.
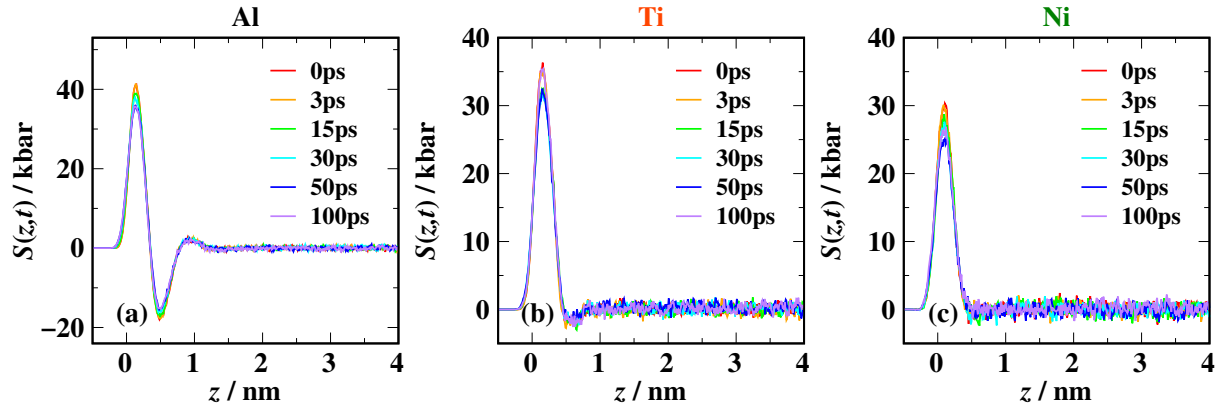
Fig.S 7. 50 ps laser pulse irradiated molten surfaces. The selected stress $S(z,t)$ profiles are aligned by the GDS of the irradiated liquid surfaces at each time.
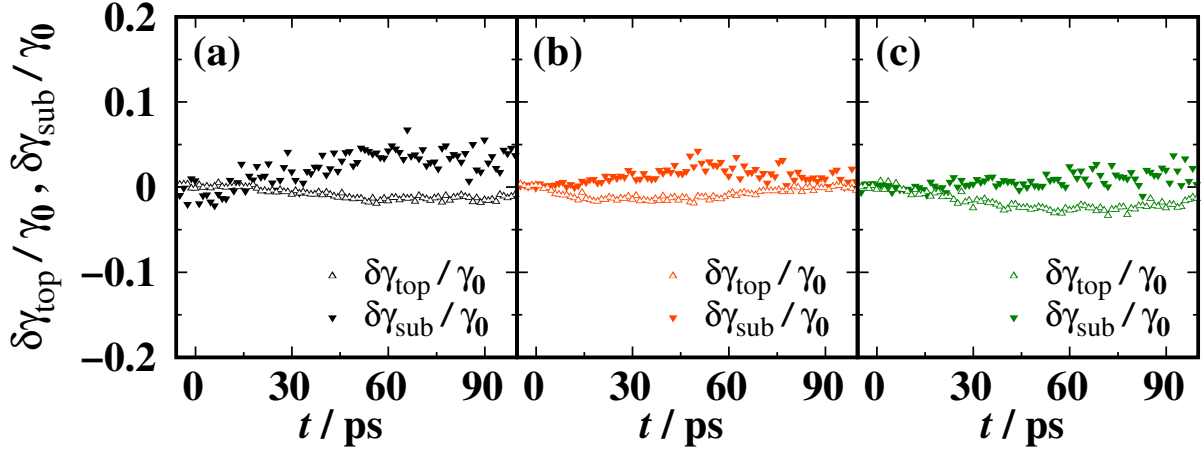
Fig.S 8. Temporal evolution of two contributing components of the dynamic surface tension, $\delta\gamma_{\text{top}}(t)/\gamma_0$ and $\delta\gamma_{\text{sub}}(t)/\gamma_0$, for the three molten surfaces irradiated with the 50 ps laser pulse. The normalization factor $\gamma_0$, are 593(2) mN/m, 1005(2) mN/m, and 892(4) mN/m, for the equilibrium Al (a), Ti (b), and Ni (c) liquid surfaces before laser irradiation. $\delta\gamma_{\text{top}}(t) = \gamma_{\text{top}}(t) - \gamma_{0\text{top}}$, $\delta\gamma_{\text{sub}}(t) = \gamma_{\text{sub}}(t) - \gamma_{0\text{sub}}$. $\gamma_{0\text{top}}$ for three equilibrium molten surfaces are Al 985(1) mN/m, Ti 1050(1) mN/m, and Ni 896(1) mN/m, respectively. Correspondingly, $\gamma_{0\text{sub}}$, Al 392(1) mN/m, Ti -45(1) mN/m, and Ni -4(3) mN/m. The presentation is as in Fig.4 in the main text.
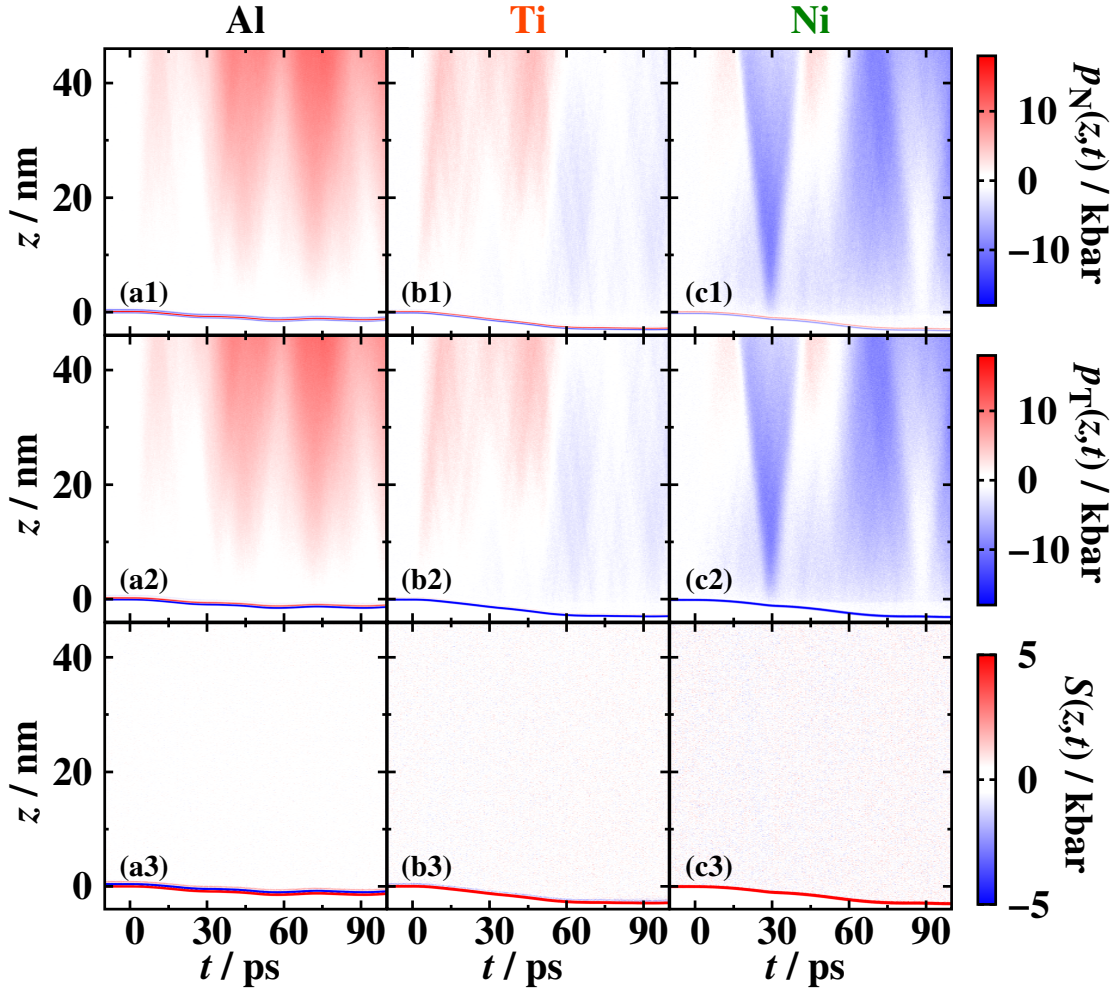
Fig.S 9. Contour plots of fine-grained profiles of the normal $(p_N(z,t))$ and transverse components $(p_T(z,t))$ of the pressure tensor, and the stress $(S(z,t))$ along the direction normal to the three molten metal surfaces irradiated with the 50 ps laser pulse. The laser pulse is directed along $z$ axis, perpendicular to the molten metal surfaces from the bottom of the contour plots. The presentation is as in Fig.5 in the main text.
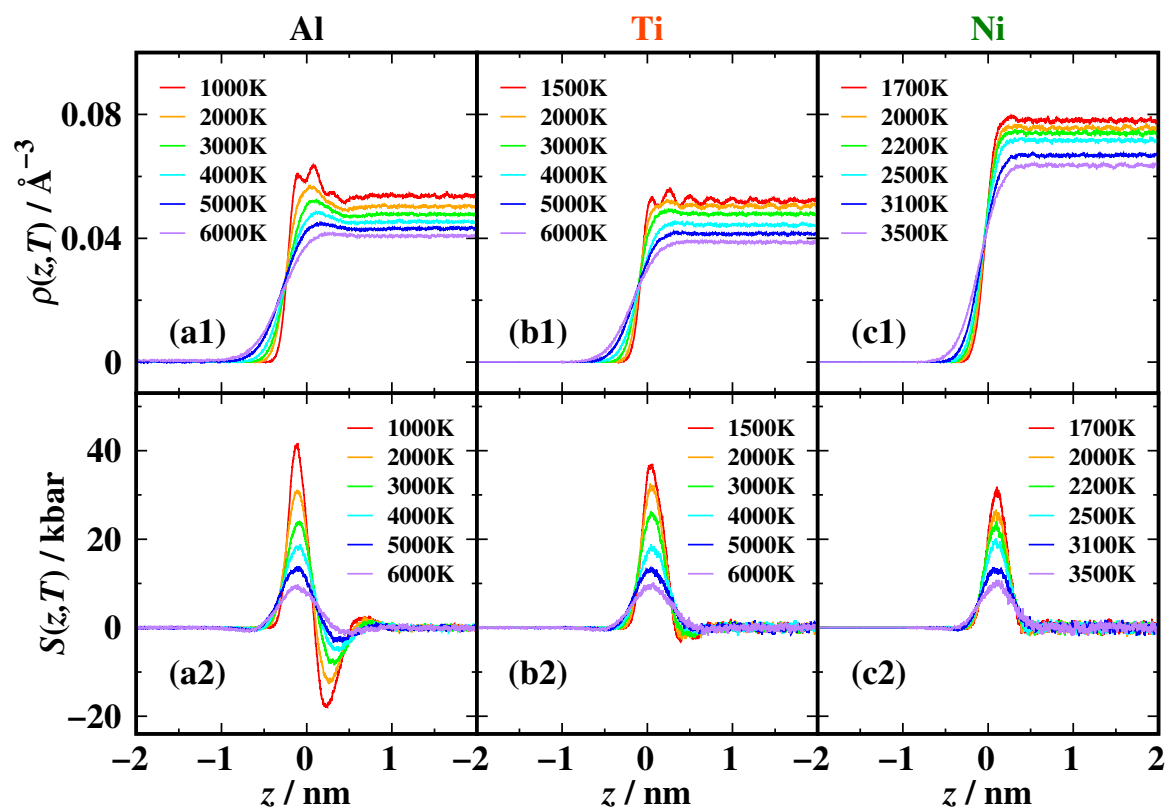
Fig.S 10. Evolution of the density $\rho(z)$ and stress $S(z)$ profiles across the equilibrium molten Al, Ti and Ni surfaces at six increasing temperatures. $z = 0$ corresponds to the GDS positions of each equilibrium molten metal surfaces.
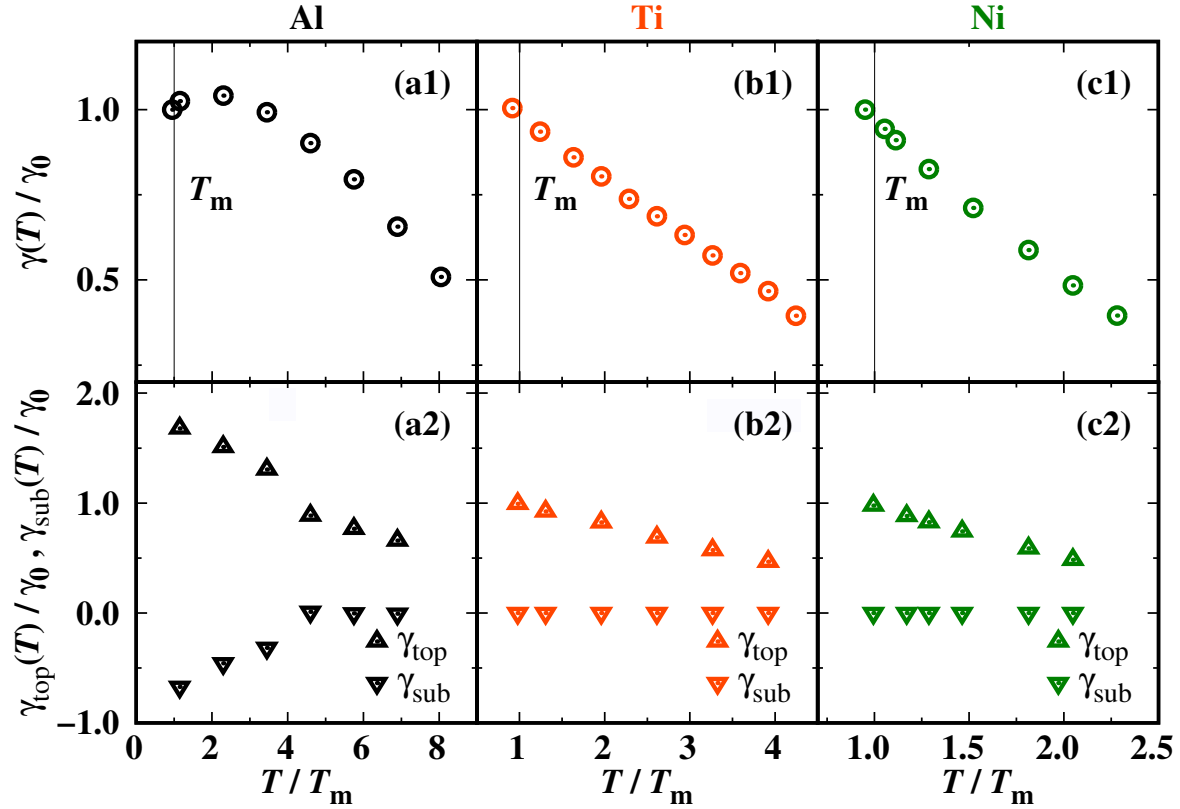
Fig.S 11. Equilibrium surface tensions of equilibrium liquid Al (a1), Ti (b1), and Ni (c1) obtained from EAM-based MD simulations as a function of temperature ranging from each 95% melting temperature up to the corresponding 70% critical temperature. The data are normalized by $\gamma_0$ of each metal system. Panels (a2-c2) plot the temperature-dependent of two (normalized) contributing components of the equilibrium surface tension, $\gamma_{\text{top}}(T)/\gamma_0$ and $\gamma_{\text{sub}}(T)/\gamma_0$, for the three molten metal surfaces under equilibrium states.
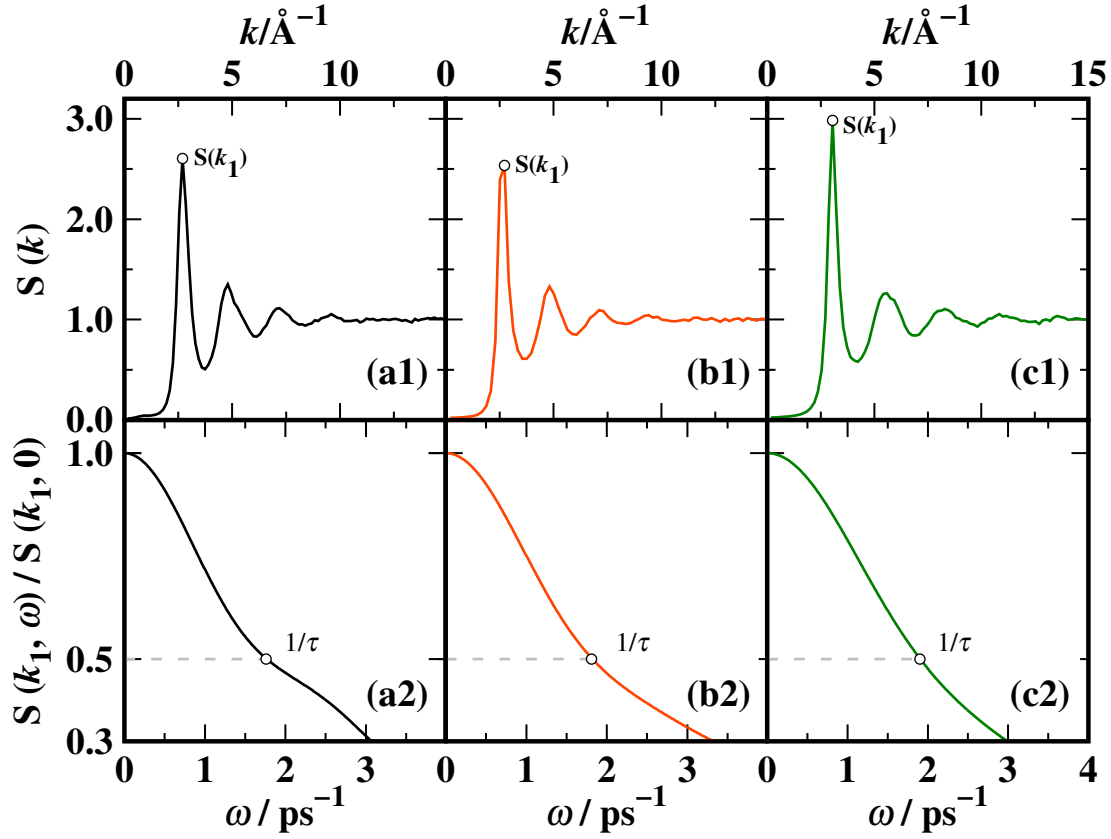
Fig.S 12. (a1)-(c1) the static structure factors $\mathbf{S}(|\vec{k}|)$ of the three molten metals (Al, Ti, Ni) under equilibrium states at each corresponding $T_{\mathrm{m}}$. (a2)-(c2) plot the dynamic structure factors normalized by their zero frequency values, $\mathbf{S}(k_1, \omega)/\mathbf{S}(k_1, 0)$. $k_1$ refers to the first peak wave number in the static structure function. The inverse $x$-axis values ($1/\omega$) denoted with an open white circle correspond to the liquid density wave relaxation times $\tau_{k_1, T_{\mathrm{m}}}$.